

# Supercell Wannier functions and a faithful low-energy model for Bernal bilayer graphene

Ammon Fischer,<sup>1,\*</sup> Lennart Klebl,<sup>2,†</sup> Dante M. Kennes,<sup>1,3</sup> and Tim O. Wehling<sup>2,4</sup>

<sup>1</sup>*Institute for Theory of Statistical Physics, RWTH Aachen University,  
and JARA Fundamentals of Future Information Technology, 52062 Aachen, Germany*

<sup>2</sup>*I. Institute for Theoretical Physics, Universität Hamburg, Notkestraße 9-11, 22607 Hamburg, Germany*

<sup>3</sup>*Max Planck Institute for the Structure and Dynamics of Matter,  
Center for Free Electron Laser Science, 22761 Hamburg, Germany*

<sup>4</sup>*The Hamburg Centre for Ultrafast Imaging, 22761 Hamburg, Germany*

(Dated: November 12, 2024)

We derive a minimal low-energy model for Bernal bilayer graphene and related rhombohedral graphene multilayers at low electronic densities by constructing Wannier orbitals defined in real-space supercells of the original primitive cell. Starting from an *ab-initio* electronic structure theory comprising the atomic carbon  $p_z$ -orbitals, momentum locality of the Fermi surface pockets around  $K$ ,  $K'$  is circumvented by backfolding the  $\pi$ -bands to the concomitant mini-Brillouin zone of the supercell, reminiscent of their (twisted) moiré counterparts. The supercell Wannier functions reproduce the spectral weight and Berry curvature of the microscopic model and offer an intuitive real-space picture of the emergent physics at low electronic densities being shaped by flavor-polarized wave packets with mesoscopic extent. By projecting an orbital-resolved, dual-gated Coulomb interaction to the effective Wannier basis, we find that the low-energy physics of Bernal bilayer graphene is governed by weak electron-electron interactions. Our study bridges between existing continuum theories and *ab-initio* studies of small Fermi pocket systems like rhombohedral graphene stacks by providing a symmetric lattice description of their low-energy physics.

**Introduction.** Since the initial experimental observation of correlated metallic and insulating states as well as superconductivity in Bernal bilayer graphene (BBG) [1, 2], numerous experimental [2–11] and theoretical efforts [12–27] have been undertaken to unravel the microscopic origin and interplay between various symmetry-broken states at low electronic densities. Experiments have shown the existence of ferromagnetic phases in the form of half- and quarter metals [1, 28], anomalous hall crystals [1], (generalized) Wigner crystals [1, 9] and superconductivity in BBG [2–4, 8] and rhombohedral trilayer graphene [29] subject to an external displacement field. Opposite to the formation of true electronic flat bands in their twisted counterparts [30–43], pristine multilayer graphene stacks host small regions in momentum space where the electronic bands are flattened upon an electrical field induced lifting of the inversion-symmetry protected Dirac points  $K^\nu$  [18, 44, 45]. This leads to the formation of van-Hove singularities on the electron and hole-doped side [7, 8], which stabilize symmetry-broken phases mediated by electron-electron interactions [1, 29]. However, the low-energy bands of multilayer graphene are neither flat in the entire Brillouin zone, nor separated from the remaining valence (conduction) bands by a well-defined energy gap. Instead, the Fermi surface near charge neutrality consists of highly localized pockets around the valleys  $K^\nu$  as shown in Fig. 1 (c).

The strategy that is commonly applied to describe the low-energy physics in BBG and related rhombohedral graphene stacks is to resort to a full momentum-space formalism by deriving a  $\mathbf{k} \cdot \mathbf{p}$  expansion of the Hamiltonian around the non-equivalent valleys  $K^\nu$  [44, 45] instead of a symmetric lattice

description. While this description is sufficient when modeling electronic properties, including the fermiology and band-structure of various multilayer graphene stacks in the presence of external fields and proximity-induced spin-orbit coupling [11, 46–49], the continuum formulation unavoidably leaves the realm of *ab-initio* theories as soon as electron-electron interactions are added to the puzzle. Truncating the model in momentum space invalidates the representation of local interaction terms and therefore hampers its applicability to well-established many-body techniques—most of which require a lattice description of the system under scrutiny including the functional renormalization group [50–52] (FRG), dynamical mean-field theory [53], or tensor network based approaches [54, 55]. The central prerequisite to first-principle motivated modeling of correlated many-body physics in small Fermi pocket systems like multilayer graphene stacks [1, 29, 56–58] or AIAs quantum wells [59, 60], is therefore the choice of a local (real-space) basis capable to account for the atomic-scale and long-wavelength physics inherent to aforementioned material candidates with nearly free electron gas behavior at low densities.

In the present manuscript, we construct a fully symmetric lattice model that captures the low-energy physics of BBG and circumvents above obstacles. We reformulate the (interacting) physics of BBG and related rhombohedral graphene stacks at low electronic densities in terms of supercell Wannier functions (SWFs) that are localized on intermediate length scales  $a_0 < L_s < 1/|q_{\text{FS}}| \sim 60a_0$  (with  $|q_{\text{FS}}|$  the characteristic extent of the Fermi pockets). By comprising several hundreds of carbon atoms on the atomic carbon-carbon scale  $a_0$ , the SWFs represent a coarse-grained description of rhombohedral graphene stacks that links the atomic representation of the electronic structure as obtained from first-principles, e.g. via density functional theory (DFT) & Wannierization

\* These authors contributed equally.; [ammon.fischer@rwth-aachen.de](mailto:ammon.fischer@rwth-aachen.de)

† These authors contributed equally.

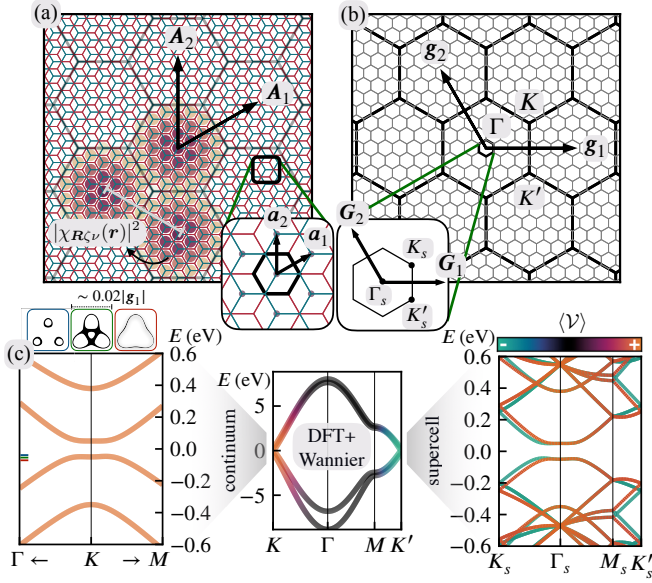


FIG. 1. Supercell Wannier construction in Bernal bilayer graphene (BBG). Real-space (a) and momentum space (b) geometry of the BBG supercell and mini Brillouin zone (BZ). The effective Wannier functions  $|\chi_{\xi^\nu}(\mathbf{r})|^2$  of the low-energy modes are localized on length scales associated to the supercell lattice constant  $L_s = |\mathbf{A}_i| = n_s |\mathbf{a}_i|$ . The original BZ is folded into the mini-BZ spanned by reciprocal lattice vectors  $\mathbf{G}_i = \mathbf{g}_i/n_s$ . The left inset shows the primitive real-space unit cell and the density of a Bloch wave packet  $\psi_K(\mathbf{r})$ . The right inset indicates the mini-BZ with its high symmetry points. (c) Bandstructure obtained from DFT & Wannierization of the carbon  $p_z$ -orbitals in the presence of an interlayer potential difference of  $\Delta = 100$  meV. Continuum limit and downfolded bands in the effective supercell are indicated as well as the Fermi surfaces across the Lifshitz transition at low densities (black markers). The bands are color-coded according to their valley expectation value  $\langle \mathcal{V} \rangle$ .

of the carbon  $p_z$ -orbitals [44] with a mesoscopic description at intermediate length scales  $L_s$ . Therefore, the SWFs yield an elegant real-space analogue of the full momentum-space formalism adopted in the continuum limit, where the locality and the effective length scales of emergent phenomena are hidden. We demonstrate that spectral features and the local Berry curvature of the valley-local flat bands near  $K^\nu$  can be faithfully represented by two  $p_\pm$ -orbitals per valley that span the  $U(4) \otimes U(4)$  symmetry space of spin, valley and layer degrees of freedom. This allows to downfold realistic (dual-gated) Coulomb interactions to the effective Wannier basis including orbitally resolved short- and long-ranged interaction components [61, 62]. Our work not only demonstrates that the low-energy physics in BBG is governed by weak electron-electron interactions, but at the same time provides a natural real-space description that bridges to the emergent physics in twisted graphene multilayers.

*Supercell construction for small Fermi pocket systems.* To circumvent a full momentum-space formalism of the low-energy physics in BBG and related small Fermi pocket systems, we propose a real-space supercell construction inspired

by the moiré pattern in twisted (graphene) multilayers [63–66], albeit without a twist between adjacent layers. For the former, Wannier models have become state of the art for studies going beyond the single-particle picture [67–73]. Instead of describing the crystal structure of BBG in terms of its primitive unit cell with Bravais lattice vectors  $\mathbf{a}_1 = (\sqrt{3}/2, 1/2)^T$  and  $\mathbf{a}_2 = (0, 1)^T$ , we set up a superlattice with rescaled lattice vectors  $\mathbf{A}_i = n_s \mathbf{a}_i$  [74], where  $n_s$  denotes the linear scaling factor of the supercell. As shown in Fig. 1 (a), the superlattice contains  $n_s^2$  primitive unit cells on the atomic scale and is characterized by the mesoscopic length scale  $L_s = |\mathbf{A}_i| = n_s |\mathbf{a}_i|$ . The associated Brillouin zone (BZ) is shrunk to a mini-BZ recovering momentum-space periodicity with respect to the reciprocal lattice vectors  $\mathbf{G}_i = \mathbf{g}_i/n_s$  as indicated in Fig. 1 (b). The high-symmetry points of the mini-BZ are labeled according to their counterparts in the primitive BZ. Depending on the choice of the scaling factor  $n_s$ , the original graphene valleys  $K^\nu$ ,  $\nu = \pm$  are mapped to either the  $\Gamma_s$ -point [ $\text{mod}(n_s, 3) = 0$ ] as shown in Fig. 1 (b), or onto the supercell  $K_s^\nu$ -points [ $\text{mod}(n_s, 3) \neq 0$ ]. To construct the Hamiltonian of the supercell from first-principles, we first consider an *ab-initio* Hamiltonian of BBG formulated in the basis of the four carbon  $p_z$ -orbitals centered at the sublattices  $X = (A_1, B_1, A_2, B_2)$  as routinely derived from DFT & Wannierization [44]. As the supercell construction itself preserves translational invariance on the carbon-carbon bond scale, the Hamiltonian associated to the primitive cell can be mapped to the supercell geometry. Hence we avoid costly DFT simulations of all  $4n_s^2$  carbon  $p_z$ -orbitals that reside within the supercell, see Supplementary Material (SM) [75] for technical details. The symmetries of the supercell Hamiltonian  $\mathcal{G}^0$  are carried over from the microscopic model, i.e.,  $\mathcal{G}^0 = C_{3v} \otimes SU(2) \otimes \mathcal{T}$ . Here,  $C_{3v}$  is the point group of the superlattice that contains a three-fold rotation around the  $z$ -axis and three vertical mirror planes, the  $SU(2)$ -symmetry acts in spin space and  $\mathcal{T}$  denotes time-reversal symmetry. At low electronic densities, the system further possesses an approximate valley conservation  $U_\nu(1)$  that is reflected in an orbital-dependent phase factor  $e^{i\mathbf{K}^\nu \mathbf{r}}$  of the respective Bloch states. In the supercell picture, the valley character of the Bloch states  $|\psi_{kb}\rangle$  can be disentangled by evaluating expectation values  $\langle \mathcal{V} \rangle = \langle \psi_{kb} | \mathcal{V} | \psi_{kb} \rangle$  of a Haldane-like operator  $\mathcal{V}$  [76, 77], see SM [75]. As demonstrated in Fig. 1 (c), the back-folded bands in the mini-BZ of the supercell originating from valley  $K^\nu$  indeed carry a well-defined expectation value  $\langle \mathcal{V} \rangle \sim \nu$ , whereas remote energy states originating from states near  $\Gamma$  show no distinct valley polarization.

The periodic supercell description of the atomic and electronic structure of BBG allows to construct a low-energy model for BBG from *first-principles* by finding a minimal Wannier representation that captures the spectral weight and Berry curvature of the valence and conduction bands near charge neutrality. In this work, we focus on the intermediate regime  $L_s < 1/|\mathbf{q}_{\text{FS}}|$ , where  $|\mathbf{q}_{\text{FS}}|$  denotes the (inverse) linear extent of the Fermi surface pockets around  $K^\nu$ . In this regime, only one band per valley contributes to the Fermi surface close

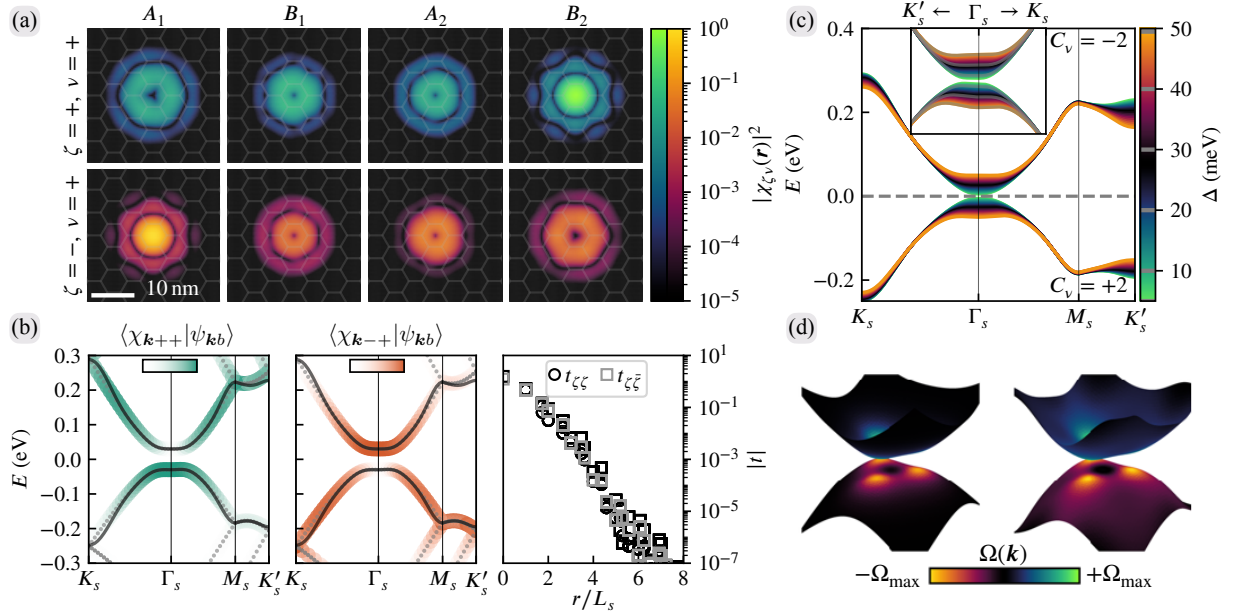


FIG. 2. Supercell Wannier orbitals and minimal low-energy model for Bernal bilayer graphene. (a) Probability density of the supercell Wannier functions (rows) on each of the four BBG sites (columns, sublattice  $A, B$  and layer 1, 2). The size of the supercell is  $n_s = 24$ , which amounts to a superlattice constant of  $|A_{1,2}| = 5.9$  nm (supercells are indicated as faint white lines). The interlayer potential difference is set to  $\Delta = 60$  meV. (b) Projection of the Wannier orbitals on the original Bloch states of the supercell model. At the supercell Gamma point  $\Gamma_s$  (that corresponds to the  $K^\nu$  points of the primitive unit cell), the two orbitals carry the pure valley character of the valence/conduction band (left/center). The dispersion is accurately reproduced (black lines: Wannier model, dotted gray lines: supercell model) in a wide region around  $\Gamma_s$ . The right panel displays intra- and inter-orbital hopping parameters of the projected Hamiltonian that both decay exponentially as a function of distance  $r$ . (c) Band structures for various displacement fields obtained from interpolating hopping parameters of the wannierized Hamiltonians for five grid points (gray markers in the colorbar). The inset shows how the interpolated Hamiltonians capture fine details of the band structure around  $\Gamma_s$  (gray lines). (d) Berry curvature in the vicinity of  $K^\nu$  in the atomic scale model of BBG (left) and the supercell Wannier model (right).

to the VHSs and the artificial length scale set by the supercell does hence not infer with emergent length scales associated to possible electronic ordering, see Fig. 1 in the SM [75]. To construct localized SWFs  $\chi_{R\zeta\nu}(\mathbf{r})$  in the presence of finite displacement fields, we apply the single-shot projection technique [68, 78, 79], see SM [75] for technical details. Choosing  $\text{mod}(n_s, 3) = 0$  allows trial wave functions  $g_{R\zeta\nu}(\mathbf{r})$  to be trivially symmetric (i.e., without phase factors) under the model's point group symmetries when sampled from Bloch states at  $\Gamma_s$ , i.e.  $g_{R\zeta\nu}(\mathbf{r}) \sim \psi_{\Gamma_s\zeta\nu}(\mathbf{r})$ . States originating from the valence (conduction) band manifold are polarized on the non-dimer orbitals  $B_2$  ( $A_1$ ) as labeled by  $\zeta = \pm$ . Due to the emergent valley conservation  $U_\nu(1)$  and the presence of time-reversal symmetry  $\mathcal{T}$  and spin- $SU(2)$  symmetry, each state at  $\Gamma_s$  is fourfold degenerate and we further separate Bloch states according to their valley polarization  $\nu = \pm$ . The trial orbitals  $g_{R\zeta\nu}(\mathbf{r})$  transform as eigenstates of  $C_{3\nu}$  with eigenvalue  $w^{\zeta\nu}$ , where  $w = e^{i2\pi/3}$ , and therefore resemble  $p_\pm = p_x \pm ip_y$ -orbitals with angular momentum  $L_z = \nu\zeta$ .

**Supercell Wannier functions.** In Fig. 2 (a) we show the valley-polarized SWFs  $\chi_{R\zeta\nu}(\mathbf{r})$  obtained in a BBG supercell with scaling factor  $n_s = 24$  and interlayer potential difference of  $\Delta = 60$  meV. However, we stress that the SWF construction presented explicitly for BBG can be generalized to arbitrary rhombohedral graphene stacks, see SM [75] for a discussion

on monolayer and ABC trilayer graphene. The SWFs are decomposed into contributions from the microscopic sublattice- and layer degrees of freedom  $X$ :  $\chi_{R\zeta\nu}(\mathbf{r}) = \{\chi_{R\zeta\nu}^X(\mathbf{r})\}$ . The amplitude of the SWF with quantum number  $\zeta$  is enhanced on the non-dimer orbital  $B_2$  ( $A_1$ ) and decays exponentially on length scales associated to the BBG supercell lattice constant  $L_s$ . To resolve the relative phase windings of the SWFs on the individual sublattices, we separate contributions of the atomic valley phase factor from the supercell envelope function  $\chi_{\zeta\nu}(\mathbf{r}) = e^{i\mathbf{K}_\nu \cdot \mathbf{r}} W_{\zeta\nu}(\mathbf{r})$ . The former features  $C_{3\nu}$  eigenvalues of  $(w^{-1}, 1, 1, w)^\nu$  on the different sublattices, whereas the supercell envelope function  $W_{\zeta\nu}(\mathbf{r})$  has eigenvalues  $(w^{(\zeta+1)}, w^\zeta, w^\zeta, w^{(\zeta-1)})^\nu$ , see SM [75]. Therefore, the total SWFs have the same  $C_{3\nu}$  eigenvalue  $w^{\zeta\nu}$  consistent with the  $p_\pm$ -orbital character of the trial functions. In particular, the sublattice components of the SWFs each have a relative phase winding of  $2 \times 2\pi$ , which is reminiscent of the wave functions of chiral quasiparticles  $\psi_{k\zeta\nu}(\mathbf{r}) \sim e^{i\mathbf{k}\cdot\mathbf{r}}(1, \zeta e^{Ji\nu\varphi_k})^T$ , where  $\varphi_k = \arg(k_x + ik_y)$  [45, 80] and  $J = 2$ . The latter are well-known to govern the low-energy physics in the continuum formulation of rhombohedral multilayer graphene [45, 80], where adiabatic propagation along a closed orbit yields a Berry phase of  $J\pi$  for  $J$ -layered rhombohedral graphene. This manifests in a half-integer valued



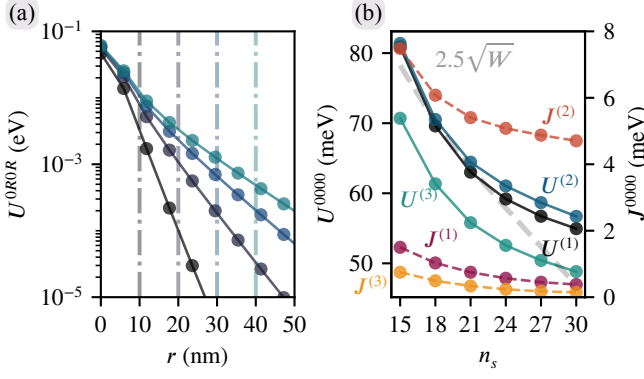


FIG. 3. Strength of Coulomb interactions in the Wannier basis. (a) Density-density vertex element  $U^{0R0R}$  as a function of distance  $r$  for various gate distances (indicated as dash-dotted vertical lines of the respective color). The supercell size is chosen as  $n_s = 24$ . (b) On-site Hubbard-Kanamori interaction components as a function of supercell size  $n_s$ . The left axis refers to Hubbard- $U$  terms and the right axis to Hund- $J$  couplings. The grey dashed line indicates the evolution of the bandwidth  $W$  of the effective model.

valley Chern number  $C_v = J\zeta\nu/2$  [81, 82] characterized by an accumulation of Berry curvature  $\Omega_v(\mathbf{k})$  in the vicinity of  $K^\nu$ . We demonstrate in Fig. 2 (d) that the SWFs accurately reproduce the Berry curvature of the original Bloch states near charge neutrality. Due to the momentum-space periodicity of the SWFs and the *connectedness* of the lowest valence (conduction) bands, the Berry curvature of the original Hamiltonian can only be captured in a constrained energy window. We find that the localized SWFs form a Haldane-like model within each valley featuring a valence (conduction) band valley Chern number  $C_v = \pm 2\nu$  and thus represent an atomic limit in each valley. As time-reversal symmetry  $\mathcal{T}$  connects different valley sectors  $\chi_{R\zeta\nu}(\mathbf{r}) = \chi_{R\zeta\nu}^*(\mathbf{r})$ , valence (conduction) bands of the full model retain Chern number  $C = 0$ . In contrast to topologically (or chirally) obstructed low-energy models [83], the SWFs capture the entire spectral weight of the Bloch states near charge neutrality. The overlaps of the SWFs with the original Bloch states satisfy  $\langle \chi_{k\zeta\nu} | \psi_{kb} \rangle = 1$  around  $\Gamma_s$  as shown in Fig. 2 (c), while decreasing at the BZ boundary. Further evidence for the valley-polarized SWFs representing an atomic limit at low densities concerns the exponential decay of the hopping parameters  $t_{(R\zeta\nu)(R'\zeta'\nu')}$  as function of distance, see the right panel of Fig. 2 (c). Due to the explicit symmetries  $U_v(1)$ ,  $\mathcal{T}$  of the low-energy model, the hopping terms fulfill  $t_{(R\zeta\nu)(R'\zeta'\nu')} = [t_{(R\zeta\nu)(R'\zeta'\nu')}]^*$  and  $t_{(R\zeta\nu)(R'\zeta'\nu')} = 0$ , such that the intra- and inter-orbital hopping terms in a single valley determine the full model. In Fig. 2 (c), we further demonstrate that the energetics of the valence (conduction) bands around charge neutrality are accurately reproduced by the SWFs. As shown in Fig. 2 (b), the effect of an external displacement field can be modeled by interpolating hopping terms at finite inter-layer potential differences, while reproducing all characteristics of the low-energy bands including trigonal warping and the size of the single-particle band gap.

*Coulomb interactions in the Wannier basis.* Besides its major advantage of a symmetric lattice description, formulating the low-energy physics of BBG in terms of SWFs has the benefit of obtaining electron-electron interactions from first principles through the intrinsic connection to the atomistic basis of carbon  $p_z$ -orbitals. We assume a realistic device geometry [1, 6], where a BBG sheet is placed inbetween hBN spacer layers of thickness  $\xi$  that determine the dielectric environment  $\epsilon \approx 4$  [23]. The hBN/BBG/hBN stack is enclosed with metallic (graphite) gates. These assumptions determine the overall strength  $\alpha/\epsilon$  and characteristic distance  $\xi$  of the long-range part of the Coulomb interaction. The short-range behavior of the Coulomb repulsion follows an Ohno form, with parameters for graphitic systems known from literature [61, 62]. This fixes the microscopic parametrization of the Coulomb interaction  $V(r)$ , see SM [75] for details. The supercell Wannier construction allows to project this first-principle  $V(r)$  to the SWF basis (see Fig. 3). First, we analyze density-density type interactions obtained by evaluating the Coulomb integral

$$U_{0R0R}^{\alpha\alpha'\alpha'} = \iint d\mathbf{r} d\mathbf{r}' |\chi_{0\alpha}(\mathbf{r})|^2 |\chi_{R\alpha'}(\mathbf{r}')|^2 V(|\mathbf{r} - \mathbf{r}'|), \quad (1)$$

for pairs of SWFs separated by  $\mathbf{R}$  in real-space. As demonstrated in Fig. 3 (a), an exponential suppression sets in for distances larger than the gate distance  $\xi = 10 \dots 40$  nm. The short-ranged terms behave like  $\sim 1/r$  when  $\xi$  is larger than the Wannier function spread. Second, we analyze the strength of local Hubbard-Kanamori interaction parameters

$$J_{0000}^{\alpha_1 \dots \alpha_4} = \iint d\mathbf{r} d\mathbf{r}' \chi_{0\alpha_1}^*(\mathbf{r}) \chi_{0\alpha_2}^*(\mathbf{r}') \times \chi_{0\alpha_4}(\mathbf{r}') \chi_{0\alpha_3}(\mathbf{r}) V(|\mathbf{r} - \mathbf{r}'|). \quad (2)$$

as well as their dependence on the supercell scaling factor  $n_s$ , see Fig. 3 (b). In the enlarged pseudospin space including spin, valley and orbital (layer) degrees of freedom, the presence of time-reversal symmetry mandates four unique types of local interactions: (i) intra-orbital ( $\zeta = \pm$  for 1, 2, respectively)  $U^{(1,2)} = U^{(\zeta\nu)(\zeta\nu)(\zeta\nu)(\zeta\nu)}$  and inter-orbital  $U^{(3)} = U^{(\zeta\nu)(\zeta\nu)(\bar{\zeta}\bar{\nu})(\bar{\zeta}\bar{\nu})}$  Hubbard interactions, (ii) inter-orbital, intra-valley coupling  $J^{(1)} = J^{(\zeta\nu)(\zeta\nu)(\zeta\nu)(\zeta\nu)}$ , (iii) intra-orbital, inter-valley coupling  $J^{(2)} = J^{(\zeta\nu)(\zeta\nu)(\bar{\zeta}\bar{\nu})(\bar{\zeta}\bar{\nu})}$  and (iv) inter-orbital and inter-valley coupling  $J^{(3)} = J^{(\zeta\nu)(\bar{\zeta}\bar{\nu})(\bar{\zeta}\bar{\nu})(\zeta\nu)}$ . The local Hubbard interaction terms scale like  $U^{(i)} \sim 1/n_s$  as expected from the Gaussian shape of the SWFs [69]. In particular, we find that for all supercell sizes  $n_s = 15 \dots 30$  considered within the scope of this work, the minimal model of BBG remains in the weakly-coupled regime  $\max_i(U^{(i)}) < W$ , where  $W$  denotes the supercell bandwidth. For the supercell scaling factor of  $n_s = 24$  used throughout the manuscript, we estimate the ratio of local interaction strength over bandwidth as  $U/W \approx 0.15$ . For  $W \gg \Delta$ , the quadratic nature of the bands leads to the ratio of Hubbard interaction over band width scaling like  $U/W \sim n_s$ . The scaling behavior of  $U/W$  changes for  $W \gtrsim \Delta$ , because the band width is not solely determined by the supercell scaling factor  $n_s$  in this case. Hund's coupling

terms are suppressed by a factor of  $\sim 10$  compared to the intra-orbital and inter-orbital Hubbard interactions. The dominant Hund's interaction term in the SWF basis is the intra-orbital, inter-valley coupling  $J^{(2)}$ .

*Discussion.* In this Letter, we introduced SWFs as an efficient representation of the low-energy physics of BBG and related rhombohedral graphene stacks. The Wannier construction is based on the atomic-scale lattice of carbon atoms, but describes the emergent low-energy physics in terms of localized, flavor-polarized supercell orbitals that have the emergent symmetries of continuum models imprinted, i.e., valley- $U(1)$ , spin- $SU(2)$  and time-reversal symmetry  $\mathcal{T}$ . To this end, we demonstrate that the spectral weight and Berry curvature of the low-energy Bloch states are faithfully represented by two valley-polarized  $p_{\pm}$ -orbitals located on the triangular sites of the superlattice. The local nature of our model implies that long-ranged Coulomb interactions can be cast into fairly local interactions, whose strength can be controlled by metallic gates. The values of the effective Coulomb interactions in the SWF basis are estimated from first principles, including density-density and exchange-type interactions like inter-valley Hund's couplings terms. The SWF construction remains valid as long as the superlattice length scale  $L_s = n_s |\mathbf{a}_i| \lesssim 1/|\mathbf{q}_{\text{FS}}|$  does not exceed the length scale associated to the width of the Fermi pockets  $|\mathbf{q}_{\text{FS}}|$  at a given electronic density. Otherwise, additional bands are back-folded to the mini-BZ and need to be wannierized in order to sufficiently model the low-energy physics. The 'three-patch' continuum model [84] proposed in the context of studying the translational symmetry-breaking anomalous Hall crystal phase [1, 82, 84, 85] can in fact be understood as special case of our microscopic SWF construction being valid in the intermediate regime  $L_s \sim 1/|\mathbf{q}_{\text{FS}}|$ , where exactly three bands contribute to the Fermi surface. Since valley conservation is included in the SWF model as an emergent symmetry, valley orders are encoded as on-site order parameters, as opposed to the microscopic picture, where the valley operator acts on bonds [86]. This natural representation of valley as a quantum number in conjunction with the substantially reduced Hilbert space of the minimal SWF model enables the study of competing correlated phenomena in the phase diagram of rhombohedral graphene stacks with unbiased weak-coupling methods like FRG [50, 51, 87] from first-principles. To this end, it may be advisable to improve the downfolding scheme of the bare, dual-gated Coulomb interactions by using constrained random-phase approximation [88] or FRG [89] schemes. Due to its strength in representing first-principle interactions, the SWF model should allow to answer pressing questions regarding the formation of superconductivity from repulsive electron-electron or attractive phonon-induced interactions in various multilayer graphene stacks. Moreover, effects like proximity-induced Ising-SOC, microscopic defects and strain can readily be included on the level of the atomistic supercell, which allows for a material-realistic description relevant for experimental setups. In addition, the SWF procedure can be extended to other graphene multilayer

stacks [26, 57, 58, 90, 91], or modulation-doped AIAs quantum wells [59, 60] featuring valley-polarized and nematic behavior at low electronic densities.

We thank Matthew T. Bunney, Francesco Grandi, and Jonas B. Profe for fruitful discussions. This work was supported by the Excellence Initiative of the German federal and state governments, the Ministry of Innovation of North Rhine-Westphalia and the Deutsche Forschungsgemeinschaft (DFG, German Research Foundation). AF and DMK acknowledge funding by the DFG under RTG 1995, within the Priority Program SPP 2244 "2DMP" – 443273985. LK and TOW gratefully acknowledge support from the DFG through FOR 5249 (QUAST, Project No. 449872909) and SPP 2244 (Project No. 422707584). TOW is supported by the Cluster of Excellence "CUI: Advanced Imaging of Matter" of the DFG (EXC 2056, Project ID 390715994). DMK acknowledges support by the Max Planck-New York City Center for Nonequilibrium Quantum Phenomena. We acknowledge computational resources provided by RWTH Aachen University under project numbers rwth1420.

- 
- [1] A. M. Seiler, F. R. Geisenhof, F. Winterer, K. Watanabe, T. Taniguchi, T. Xu, F. Zhang, and R. T. Weitz, Quantum cascade of correlated phases in trigonally warped bilayer graphene, *Nature* **608**, 298 (2022).
  - [2] H. Zhou, L. Holleis, Y. Saito, L. Cohen, W. Huynh, C. L. Patterson, F. Yang, T. Taniguchi, K. Watanabe, and A. F. Young, Isospin magnetism and spin-polarized superconductivity in bernal bilayer graphene, *Science* **375**, 774 (2022).
  - [3] L. Holleis, C. L. Patterson, Y. Zhang, H. M. Yoo, H. Zhou, T. Taniguchi, K. Watanabe, S. Nadj-Perge, and A. F. Young, Ising superconductivity and nematicity in bernal bilayer graphene with strong spin orbit coupling (2023), [arXiv:2303.00742 \[cond-mat.supr-con\]](https://arxiv.org/abs/2303.00742).
  - [4] Y. Zhang, R. Polski, A. Thomson, É. Lantagne-Hurtubise, C. Lewandowski, H. Zhou, K. Watanabe, T. Taniguchi, J. Alicea, and S. Nadj-Perge, Enhanced superconductivity in spin-orbit proximitized bilayer graphene, *Nature* **613**, 268 (2023).
  - [5] F. Winterer, F. R. Geisenhof, N. Fernandez, A. M. Seiler, F. Zhang, and R. T. Weitz, Ferroelectric and anomalous quantum hall states in bare rhombohedral trilayer graphene (2023), [arXiv:2305.04950 \[cond-mat.mes-hall\]](https://arxiv.org/abs/2305.04950).
  - [6] A. M. Seiler, M. Statz, I. Weimer, N. Jacobsen, K. Watanabe, T. Taniguchi, Z. Dong, L. S. Levitov, and R. T. Weitz, Interaction-driven (quasi-) insulating ground states of gapped electron-doped bilayer graphene (2023), [arXiv:2308.00827 \[cond-mat.str-el\]](https://arxiv.org/abs/2308.00827).
  - [7] A. M. Seiler, Y. Zhumagulov, K. Zollner, C. Yoon, D. Urbaniak, F. R. Geisenhof, K. Watanabe, T. Taniguchi, J. Fabian, F. Zhang, *et al.*, Layer-selective spin-orbit coupling and strong correlation in bilayer graphene, *arXiv preprint arXiv:2403.17140* (2024).
  - [8] C. Li, F. Xu, B. Li, J. Li, G. Li, K. Watanabe, T. Taniguchi, B. Tong, J. Shen, L. Lu, J. Jia, F. Wu, X. Liu, and T. Li, Tunable superconductivity in electron- and hole-doped bernal bilayer graphene (2024), [arXiv:2405.04479 \[cond-mat.supr-con\]](https://arxiv.org/abs/2405.04479).
  - [9] Y.-C. Tsui, M. He, Y. Hu, E. Lake, T. Wang, K. Watanabe, T. Taniguchi, M. P. Zaletel, and A. Yazdani, Direct observation of a magnetic-field-induced wigner crystal, *Nature* **628**, 287

- (2024).
- [10] T. Xie, T. M. Wolf, S. Xu, Z. Cui, R. Xiong, Y. Ou, P. Hays, L. F. Holleis, Y. Guo, O. I. Sheekey, C. Patterson, T. Arp, K. Watanabe, T. Taniguchi, S. A. Tongay, A. F. Young, A. H. MacDonald, and C. Jin, Optical imaging of flavor order in flat band graphene (2024), [arXiv:2405.08074 \[cond-mat.mes-hall\]](#).
  - [11] A. M. Seiler, Y. Zhumagulov, K. Zollner, C. Yoon, D. Urbaniak, F. R. Geisenhof, K. Watanabe, T. Taniguchi, J. Fabian, F. Zhang, and R. T. Weitz, Layer-selective spin-orbit coupling and strong correlation in bilayer graphene (2024), [arXiv:2403.17140 \[cond-mat.mes-hall\]](#).
  - [12] S. Chatterjee, T. Wang, E. Berg, and M. P. Zaletel, Inter-valley coherent order and isospin fluctuation mediated superconductivity in rhombohedral trilayer graphene, *Nature Communications* **13**, 6013 (2022).
  - [13] A. L. Szabó and B. Roy, Competing orders and cascade of degeneracy lifting in doped bernal bilayer graphene, *Physical Review B* **105**, L201107 (2022).
  - [14] A. L. Szabó and B. Roy, Metals, fractional metals, and superconductivity in rhombohedral trilayer graphene, *Physical Review B* **105**, L081407 (2022).
  - [15] Y.-Z. You and A. Vishwanath, Kohn-luttinger superconductivity and intervalley coherence in rhombohedral trilayer graphene, *Phys. Rev. B* **105**, 134524 (2022).
  - [16] Z. Li, X. Kuang, A. Jimeno-Pozo, H. Sainz-Cruz, Z. Zhan, S. Yuan, and F. Guinea, Charge fluctuations, phonons and superconductivity in multilayer graphene, *arXiv preprint arXiv:2303.17286* (2023).
  - [17] P. A. Pantaleón, A. Jimeno-Pozo, H. Sainz-Cruz, T. Cea, V. T. Phong, and F. Guinea, Superconductivity and correlated phases in bilayer, trilayer graphene and related structures, *arXiv preprint arXiv:2211.02880* (2022).
  - [18] P. A. Pantaleón, A. Jimeno-Pozo, H. Sainz-Cruz, V. T. Phong, T. Cea, and F. Guinea, Superconductivity and correlated phases in non-twisted bilayer and trilayer graphene, *Nature Reviews Physics*, 1 (2023).
  - [19] T. Cea, P. A. Pantaleón, V. T. Phong, and F. Guinea, Superconductivity from repulsive interactions in rhombohedral trilayer graphene: A kohn-luttinger-like mechanism, *Physical Review B* **105**, 075432 (2022).
  - [20] A. Jimeno-Pozo, H. Sainz-Cruz, T. Cea, P. A. Pantaleón, and F. Guinea, Superconductivity from electronic interactions and spin-orbit enhancement in bilayer and trilayer graphene, *Physical Review B* **107**, L161106 (2023).
  - [21] T. Cea, Superconductivity induced by the intervalley coulomb scattering in a few layers of graphene, *Phys. Rev. B* **107**, L041111 (2023).
  - [22] H. Dai, R. Ma, X. Zhang, and T. Ma, Quantum monte carlo study of superconductivity in rhombohedral trilayer graphene under an electric field (2022), [arXiv:2204.06222 \[cond-mat.str-el\]](#).
  - [23] A. Ghazaryan, T. Holder, E. Berg, and M. Serbyn, Multilayer graphenes as a platform for interaction-driven physics and topological superconductivity, *Physical Review B* **107**, 104502 (2023).
  - [24] W. Qin, C. Huang, T. Wolf, N. Wei, I. Blinov, and A. H. MacDonald, Functional renormalization group study of superconductivity in rhombohedral trilayer graphene, *Phys. Rev. Lett.* **130**, 146001 (2023).
  - [25] G. Wagner, Y. H. Kwan, N. Bultinck, S. H. Simon, and S. Parameswaran, Superconductivity from repulsive interactions in bernal-stacked bilayer graphene, *arXiv preprint arXiv:2302.00682* (2023).
  - [26] A. Fischer, L. Klebl, J. B. Profe, A. Rothstein, L. Waldecker, B. Beschoten, T. O. Wehling, and D. M. Kennes, Spin and charge fluctuation induced pairing in abcb tetralayer graphene, *Physical Review Research* **6**, L012003 (2024).
  - [27] Y. Zhumagulov, D. Kochan, and J. Fabian, Emergent correlated phases in rhombohedral trilayer graphene induced by proximity spin-orbit and exchange coupling (2023), [arXiv:2305.14277 \[cond-mat.str-el\]](#).
  - [28] H. Zhou, T. Xie, A. Ghazaryan, T. Holder, J. R. Ehrets, E. M. Spanton, T. Taniguchi, K. Watanabe, E. Berg, M. Serbyn, *et al.*, Half-and quarter-metals in rhombohedral trilayer graphene, *Nature* **598**, 429 (2021).
  - [29] H. Zhou, T. Xie, T. Taniguchi, K. Watanabe, and A. F. Young, Superconductivity in rhombohedral trilayer graphene, *Nature* **598**, 434 (2021).
  - [30] Y. Cao, V. Fatemi, S. Fang, K. Watanabe, T. Taniguchi, E. Kaxiras, and P. Jarillo-Herrero, Unconventional superconductivity in magic-angle graphene superlattices, *Nature* **556**, 43 (2018).
  - [31] M. Yankowitz, S. Chen, H. Polshyn, Y. Zhang, K. Watanabe, T. Taniguchi, D. Graf, A. F. Young, and C. R. Dean, Tuning superconductivity in twisted bilayer graphene, *Science* **363**, 1059 (2019).
  - [32] X. Lu, P. Stepanov, W. Yang, M. Xie, M. A. Aamir, I. Das, C. Urgell, K. Watanabe, T. Taniguchi, G. Zhang, *et al.*, Superconductors, orbital magnets and correlated states in magic-angle bilayer graphene, *Nature* **574**, 653 (2019).
  - [33] Y. Saito, J. Ge, K. Watanabe, T. Taniguchi, and A. F. Young, Independent superconductors and correlated insulators in twisted bilayer graphene, *Nature Physics* **16**, 926 (2020).
  - [34] P. Stepanov, I. Das, X. Lu, A. Fahimniya, K. Watanabe, T. Taniguchi, F. H. Koppens, J. Lischner, L. Levitov, and D. K. Efetov, Untying the insulating and superconducting orders in magic-angle graphene, *Nature* **583**, 375 (2020).
  - [35] M. Oh, K. P. Nuckolls, D. Wong, R. L. Lee, X. Liu, K. Watanabe, T. Taniguchi, and A. Yazdani, Evidence for unconventional superconductivity in twisted bilayer graphene, *Nature* **600**, 240 (2021).
  - [36] Y. Cao, D. Rodan-Legrain, J. M. Park, N. F. Yuan, K. Watanabe, T. Taniguchi, R. M. Fernandes, L. Fu, and P. Jarillo-Herrero, Nematicity and competing orders in superconducting magic-angle graphene, *science* **372**, 264 (2021).
  - [37] Y. Zhang, R. Polski, C. Lewandowski, A. Thomson, Y. Peng, Y. Choi, H. Kim, K. Watanabe, T. Taniguchi, J. Alicea, *et al.*, Ascendancy of superconductivity in magic-angle graphene multilayers, *arXiv preprint arXiv:2112.09270* (2021).
  - [38] J. M. Park, Y. Cao, K. Watanabe, T. Taniguchi, and P. Jarillo-Herrero, Tunable strongly coupled superconductivity in magic-angle twisted trilayer graphene, *Nature* **590**, 249 (2021).
  - [39] Y. Cao, J. M. Park, K. Watanabe, T. Taniguchi, and P. Jarillo-Herrero, Pauli-limit violation and re-entrant superconductivity in moiré graphene, *Nature* **595**, 526 (2021).
  - [40] H. Kim, Y. Choi, C. Lewandowski, A. Thomson, Y. Zhang, R. Polski, K. Watanabe, T. Taniguchi, J. Alicea, and S. Nadj-Perge, Evidence for unconventional superconductivity in twisted trilayer graphene, *Nature* **606**, 494 (2022).
  - [41] X. Liu, N. J. Zhang, K. Watanabe, T. Taniguchi, and J. Li, Isospin order in superconducting magic-angle twisted trilayer graphene, *Nature Physics* **18**, 522 (2022).
  - [42] A. Kerelsky, L. J. McGilly, D. M. Kennes, L. Xian, M. Yankowitz, S. Chen, K. Watanabe, T. Taniguchi, J. Hone, C. Dean, *et al.*, Maximized electron interactions at the magic angle in twisted bilayer graphene, *Nature* **572**, 95 (2019).
  - [43] L. Balents, C. R. Dean, D. K. Efetov, and A. F. Young, Superconductivity and strong correlations in moiré flat bands, *Nature Physics* **16**, 725 (2020).



- [44] J. Jung and A. H. MacDonald, Accurate tight-binding models for the  $\pi$  bands of bilayer graphene, *Physical Review B* **89**, 035405 (2014).
- [45] A. V. Rozhkov, A. Sboychakov, A. Rakhmanov, and F. Nori, Electronic properties of graphene-based bilayer systems, *Physics Reports* **648**, 1 (2016).
- [46] M. Gmitra, S. Konschuh, C. Ertler, C. Ambrosch-Draxl, and J. Fabian, Band-structure topologies of graphene: Spin-orbit coupling effects from first principles, *Physical Review B* **80**, 235431 (2009).
- [47] M. Gmitra and J. Fabian, Graphene on transition-metal dichalcogenides: A platform for proximity spin-orbit physics and optospintronics, *Physical Review B* **92**, 155403 (2015).
- [48] K. Zollner, M. Gmitra, T. Frank, and J. Fabian, Theory of proximity-induced exchange coupling in graphene on hbn/(co, ni), *Physical Review B* **94**, 155441 (2016).
- [49] J. F. Sierra, J. Fabian, R. K. Kawakami, S. Roche, and S. O. Valenzuela, Van der waals heterostructures for spintronics and opto-spintronics, *Nature Nanotechnology* **16**, 856 (2021).
- [50] W. Metzner, M. Salmhofer, C. Honerkamp, V. Meden, and K. Schönhammer, Functional renormalization group approach to correlated fermion systems, *Rev. Mod. Phys.* **84**, 299 (2012).
- [51] C. Platt, W. Hanke, and R. Thomale, Functional renormalization group for multi-orbital fermi surface instabilities, *Advances in Physics* **62**, 453 (2013).
- [52] C. Honerkamp, Density waves and cooper pairing on the honeycomb lattice, *Phys. Rev. Lett.* **100**, 146404 (2008).
- [53] A. Georges, G. Kotliar, W. Krauth, and M. J. Rozenberg, Dynamical mean-field theory of strongly correlated fermion systems and the limit of infinite dimensions, *Reviews of Modern Physics* **68**, 13 (1996).
- [54] U. Schollwöck, The density-matrix renormalization group in the age of matrix product states, *Annals of physics* **326**, 96 (2011).
- [55] R. Orús, A practical introduction to tensor networks: Matrix product states and projected entangled pair states, *Annals of physics* **349**, 117 (2014).
- [56] L. Banszerus, S. Möller, K. Hecker, E. Icking, K. Watanabe, T. Taniguchi, F. Hassler, C. Volk, and C. Stampfer, Particle-hole symmetry protects spin-valley blockade in graphene quantum dots, *Nature*, 1 (2023).
- [57] K. G. Wirth, J. B. Profe, A. Rothstein, H. Kyoseva, D. Siebenkotten, L. Conrads, L. Klebl, A. Fischer, B. Beschoten, C. Stampfer, D. M. Kennes, L. Waldecker, and T. Taubner, Experimental Observation of ABCB Stacked Tetralayer Graphene, *ACS Nano* **16**, 16617 (2022).
- [58] S. S. Atri, W. Cao, B. Alon, N. Roy, M. V. Stern, V. Falko, M. Goldstein, L. Kronik, M. Urbakh, O. Hod, and M. B. Shalom, Spontaneous electric polarization in graphene polytypes (2023), [arXiv:2305.10890](https://arxiv.org/abs/2305.10890) [cond-mat.mtrl-sci].
- [59] M. S. Hossain, M. K. Ma, K. A. Villegas-Rosales, Y. J. Chung, L. N. Pfeiffer, K. W. West, K. W. Baldwin, and M. Shayegan, Spontaneous valley polarization of itinerant electrons, *Phys. Rev. Lett.* **127**, 116601 (2021).
- [60] Y. P. Shkolnikov, E. P. De Poortere, E. Tutuc, and M. Shayegan, Valley splitting of two-dimensional electrons in a perpendicular magnetic field, *Phys. Rev. Lett.* **89**, 226805 (2002).
- [61] T. O. Wehling, E. Şaşıoğlu, C. Friedrich, A. I. Lichtenstein, M. I. Katsnelson, and S. Blügel, Strength of effective coulomb interactions in graphene and graphite, *Phys. Rev. Lett.* **106**, 236805 (2011).
- [62] M. Rösner, E. Şaşıoğlu, C. Friedrich, S. Blügel, and T. Wehling, Wannier function approach to realistic coulomb interactions in layered materials and heterostructures, *Physical Review B* **92**, 085102 (2015).
- [63] R. Bistritzer and A. H. MacDonald, Moiré bands in twisted double-layer graphene, *Proceedings of the National Academy of Sciences* **108**, 12233 (2011).
- [64] J. L. Dos Santos, N. Peres, and A. C. Neto, Graphene bilayer with a twist: Electronic structure, *Physical review letters* **99**, 256802 (2007).
- [65] S. Shallcross, S. Sharma, E. Kandelaki, and O. Pankratov, Electronic structure of turbostratic graphene, *Physical Review B* **81**, 165105 (2010).
- [66] E. S. Morell, J. Correa, P. Vargas, M. Pacheco, and Z. Barticevic, Flat bands in slightly twisted bilayer graphene: Tight-binding calculations, *Physical Review B* **82**, 121407 (2010).
- [67] S. Carr, S. Fang, Z. Zhu, and E. Kaxiras, Exact continuum model for low-energy electronic states of twisted bilayer graphene, *Phys. Rev. Res.* **1**, 013001 (2019).
- [68] S. Carr, S. Fang, H. C. Po, A. Vishwanath, and E. Kaxiras, Derivation of wannier orbitals and minimal-basis tight-binding hamiltonians for twisted bilayer graphene: First-principles approach, *Phys. Rev. Res.* **1**, 033072 (2019).
- [69] Z.-D. Song and B. A. Bernevig, Magic-angle twisted bilayer graphene as a topological heavy fermion problem, *Physical review letters* **129**, 047601 (2022).
- [70] H. Hu, G. Rai, L. Crippa, J. Herzog-Arbeitman, D. Călugăru, T. Wehling, G. Sangiovanni, R. Valentí, A. M. Tsvelik, and B. A. Bernevig, Symmetric kondo lattice states in doped strained twisted bilayer graphene, *Phys. Rev. Lett.* **131**, 166501 (2023).
- [71] J. Yu, M. Xie, B. A. Bernevig, and S. Das Sarma, Magic-angle twisted symmetric trilayer graphene as a topological heavy-fermion problem, *Phys. Rev. B* **108**, 035129 (2023).
- [72] G. Rai, L. Crippa, D. Călugăru, H. Hu, L. de' Medici, A. Georges, B. A. Bernevig, R. Valentí, G. Sangiovanni, and T. Wehling, *Dynamical correlations and order in magic-angle twisted bilayer graphene* (2023), [arXiv:2309.08529](https://arxiv.org/abs/2309.08529) [cond-mat.str-el].
- [73] D. Bennett, D. T. Larson, L. Sharma, S. Carr, and E. Kaxiras, Twisted bilayer graphene revisited: Minimal two-band model for low-energy bands, *Phys. Rev. B* **109**, 155422 (2024).
- [74] In principle, the construction works for all supercells that are the result of a linear integer map applied to the primitive lattice vectors, i.e.,  $(\mathbf{A}_1, \mathbf{A}_2)^T = \mathcal{N} \cdot (\mathbf{a}_1, \mathbf{a}_2)^T$ , with  $\mathcal{N}$  a  $2 \times 2$  matrix with integer entries.
- [75] See Supplementary Material at [URL will be inserted by publisher] for details on the construction of supercell Wannier Hamiltonians, supercell Wannierization via single-shot projection, supercell Wannier functions for (i) Bernal bilayer graphene, (ii) monolayer graphene, (iii) rhombohedral (ABC) trilayer graphene, dual-gated Ohno-Coulomb interaction, and valley as a quantum number; including Refs. [1, 6, 23, 44, 61, 68, 77, 78, 88, 89, 92–97].
- [76] F. D. M. Haldane, Model for a quantum hall effect without landau levels: Condensed-matter realization of the "parity anomaly", *Physical Review Letters* **61**, 2015 (1988).
- [77] A. Ramires and J. L. Lado, Electrically tunable gauge fields in tiny-angle twisted bilayer graphene, *Physical review letters* **121**, 146801 (2018).
- [78] N. Marzari and D. Vanderbilt, Maximally localized generalized wannier functions for composite energy bands, *Physical review B* **56**, 12847 (1997).
- [79] J. Kang and O. Vafek, Strong coupling phases of partially filled twisted bilayer graphene narrow bands, *Phys. Rev. Lett.* **122**, 246401 (2019).
- [80] E. McCann and V. I. Fal'ko, Landau-level degeneracy and quantum hall effect in a graphite bilayer, *Physical review letters* **96**, 086805 (2006).

- [81] F. Zhang, A. H. MacDonald, and E. J. Mele, Valley chern numbers and boundary modes in gapped bilayer graphene, *Proceedings of the National Academy of Sciences* **110**, 10546 (2013).
- [82] J. Herzog-Arbeitman, Y. Wang, J. Liu, P. M. Tam, Z. Qi, Y. Jia, D. K. Efetov, O. Vafek, N. Regnault, H. Weng, Q. Wu, B. A. Bernevig, and J. Yu, Moiré fractional chern insulators. ii. first-principles calculations and continuum models of rhombohedral graphene superlattices, *Phys. Rev. B* **109**, 205122 (2024).
- [83] J. Herzog-Arbeitman, J. Yu, D. Călugăru, H. Hu, N. Regnault, C. Liu, S. D. Sarma, O. Vafek, P. Coleman, A. Tsvelik, Z. da Song, and B. A. Bernevig, Topological heavy fermion principle for flat (narrow) bands with concentrated quantum geometry (2024), [arXiv:2404.07253 \[cond-mat.str-el\]](#).
- [84] T. Soejima, J. Dong, T. Wang, T. Wang, M. P. Zaletel, A. Vishwanath, and D. E. Parker, Anomalous hall crystals in rhombohedral multilayer graphene ii: General mechanism and a minimal model (2024), [arXiv:2403.05522 \[cond-mat.str-el\]](#).
- [85] Y. Zeng, T. M. R. Wolf, C. Huang, N. Wei, S. A. A. Ghorashi, A. H. MacDonald, and J. Cano, Gate-tunable topological phases in superlattice modulated bilayer graphene (2024), [arXiv:2401.04321 \[cond-mat.mes-hall\]](#).
- [86] Using valley as a quantum number in the supercell model amounts to convoluting the  $q = 0$  valley operator with a  $q = G_s$  charge density wave, see SM [75].
- [87] J. B. Profe, D. M. Kennes, and L. Klebl, divERGE implements various Exact Renormalization Group examples, *SciPost Phys. Codebases*, 26 (2024).
- [88] F. Aryasetiawan, M. Imada, A. Georges, G. Kotliar, S. Biermann, and A. Lichtenstein, Frequency-dependent local interactions and low-energy effective models from electronic structure calculations, *Physical Review B* **70**, 195104 (2004).
- [89] M. Kinza and C. Honerkamp, Low-energy effective interactions beyond the constrained random-phase approximation by the functional renormalization group, *Phys. Rev. B* **92**, 045113 (2015).
- [90] A. Garcia-Ruiz, V. Enaldiev, A. McEllistim, and V. I. Fal'ko, Mixed-stacking few-layer graphene as an elemental weak ferroelectric material, *Nano Letters* **23**, 4120 (2023).
- [91] A. McEllistim, A. Garcia-Ruiz, Z. A. Goodwin, and V. I. Fal'ko, Spectroscopic signatures of tetralayer graphene poltypes, *Physical Review B* **107**, 155147 (2023).
- [92] M. Kang, S. Fang, L. Ye, H. C. Po, J. Denlinger, C. Jozwiak, A. Bostwick, E. Rotenberg, E. Kaxiras, J. G. Checkelsky, and R. Comin, Topological flat bands in frustrated kagome lattice CoSn, *Nature Communications* **11**, 4004 (2020).
- [93] K. Koepernik, O. Janson, Y. Sun, and J. Van Den Brink, Symmetry-conserving maximally projected wannier functions, *Physical Review B* **107**, 235135 (2023).
- [94] I. Souza, N. Marzari, and D. Vanderbilt, Maximally localized wannier functions for entangled energy bands, *Phys. Rev. B* **65**, 035109 (2001).
- [95] R. E. Throckmorton and O. Vafek, Fermions on bilayer graphene: Symmetry breaking for  $b=0$  and  $v=0$ , *Physical Review B* **86**, 115447 (2012).
- [96] A. A. Mostofi, J. R. Yates, Y.-S. Lee, I. Souza, D. Vanderbilt, and N. Marzari, wannier90: A tool for obtaining maximally-localised wannier functions, *Computer physics communications* **178**, 685 (2008).
- [97] F. Zhang, B. Sahu, H. Min, and A. H. MacDonald, Band structure of *abc*-stacked graphene trilayers, *Phys. Rev. B* **82**, 035409 (2010).



# Supplementary Material: Supercell Wannier functions and a faithful low-energy model for Bernal bilayer graphene

Ammon Fischer,<sup>1,\*</sup> Lennart Klebl,<sup>2,\*</sup> Dante M. Kennes,<sup>1,3</sup> and Tim O. Wehling<sup>2,4</sup>

<sup>1</sup>*Institute for Theory of Statistical Physics, RWTH Aachen University,  
and JARA Fundamentals of Future Information Technology, 52062 Aachen, Germany*

<sup>2</sup>*I. Institute for Theoretical Physics, Universität Hamburg, NotkestraSe 9-11, 22607 Hamburg, Germany*

<sup>3</sup>*Max Planck Institute for the Structure and Dynamics of Matter,  
Center for Free Electron Laser Science, 22761 Hamburg, Germany*

<sup>4</sup>*The Hamburg Centre for Ultrafast Imaging, 22761 Hamburg, Germany*

(Dated: November 9, 2024)

## CONTENTS

I. Construction of the supercell Hamiltonian from first principles	1
II. Supercell Wannierization via single-shot projection	2
III. Supercell Wannier functions for Bernal bilayer graphene	3
IV. Supercell Wannier functions for monolayer graphene	4
V. Supercell wannier functions for rhombohedral (ABC) trilayer graphene	5
VI. Dual-gated Ohno-Coulomb interaction	5
VII. Valley as quantum number	7
References	8

## I. CONSTRUCTION OF THE SUPERCELL HAMILTONIAN FROM FIRST PRINCIPLES

The microscopic Hamiltonian for Bernal bilayer graphene (BBG) is taken from Ref. [44] and is obtained from first principles via density functional theory (DFT) and successive Wannierization of the carbon  $p_z$ -orbitals located at the sublattices  $X \in \{A_1, B_1, A_2, B_2\}$  within the primitive cell. The carbon  $p_z$ -orbitals are located at  $\tau_{A_1} = \frac{1}{3}\mathbf{a}_1 + \frac{1}{3}\mathbf{a}_2$ ,  $\tau_{B_1} = \frac{2}{3}\mathbf{a}_1 + \frac{2}{3}\mathbf{a}_2$ ,  $\tau_{A_2} = \frac{1}{3}\mathbf{a}_1 + \frac{1}{3}\mathbf{a}_2 + \tau_2 + d\mathbf{e}_z$  and  $\tau_{B_2} = \frac{2}{3}\mathbf{a}_1 + \frac{2}{3}\mathbf{a}_2 + \tau_2 + d\mathbf{e}_z$  within the primitive cell. Here,  $\mathbf{a}_1 = (\sqrt{3}/2, 1/2)^T$  and  $\mathbf{a}_2 = (0, 1)^T$  labels Bravais lattice vectors of the real-space primitive cell,  $d$  denotes the interlayer distance of bilayer graphene [44] and  $\tau_2 = \frac{1}{3}\mathbf{a}_1 + \frac{1}{3}\mathbf{a}_2$  is the lateral shift of the first layer with respect to the second layer. We further model the presence of an external displacement field  $\Delta$  that lifts the inversion symmetry via the following term in the Hamiltonian:

$$H_\Delta = \frac{\Delta}{2} \sum_{\mathbf{r}} \left( c_{\mathbf{r},A_1}^\dagger c_{\mathbf{r},A_1} + c_{\mathbf{r},B_1}^\dagger c_{\mathbf{r},B_1} - c_{\mathbf{r},A_2}^\dagger c_{\mathbf{r},A_2} - c_{\mathbf{r},B_2}^\dagger c_{\mathbf{r},B_2} \right), \quad (1)$$

where  $\mathbf{r} = n_1\mathbf{a}_1 + n_2\mathbf{a}_2$  labels translations of the primitive unit cell. The microscopic Hamiltonian is extended to the superlattice with re-scaled lattice vectors  $\mathbf{A}_i = n_i\mathbf{a}_i$  by exploiting translational invariance on the two length scales, i.e., the carbon-carbon scale  $\delta = n_1\mathbf{a}_1 + n_2\mathbf{a}_2$ ,  $n_i \in \{0, \dots, n_s - 1\}$  and the supercell scale  $\Delta = \tilde{n}_1\mathbf{A}_1 + \tilde{n}_2\mathbf{A}_2$ ,  $\tilde{n}_i \in \mathbb{Z}$ . To this end, we may write the microscopic Hamiltonian as

$$H_{XX'}(\mathbf{k}) = \sum_{\Delta, \delta} e^{-ik(\Delta + \delta)} t_{XX'}(\Delta + \delta), \quad H = \sum_{\mathbf{k}, X, X'} c_{\mathbf{k}, X}^\dagger H_{XX'}(\mathbf{k}) c_{\mathbf{k}, X'}, \quad (2)$$

---

\* These authors contributed equally.

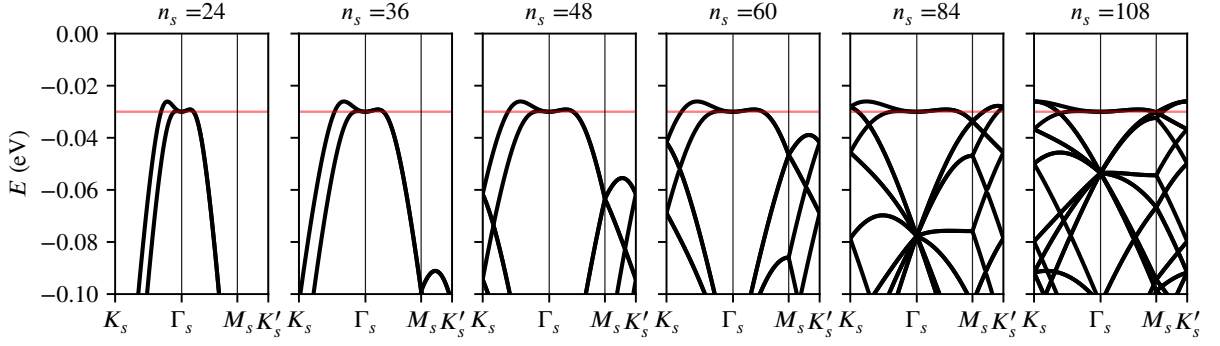


FIG. 1. Supercell bandstructure obtained for different scaling factors  $n_s$  in the presence of an interlayer potential difference of  $\Delta = 60$  meV. The red horizontal line indicates the position of the VHS.

where  $\mathbf{k}$  refers to crystal momenta in the first Brillouin zone (BZ) of the microscopic lattice, and  $t_{XX'}(\delta)$  are the hopping elements of the original (microscopic) Wannier Hamiltonian given in Ref. [44]. An inverse Fourier transform on the microscopic scale associated with  $(\delta, \mathbf{k})$  yields the elements of the supercell Hamiltonian at mini-BZ momentum  $\mathbf{K}$ :

$$\begin{aligned}
 H_{X,X'+\delta}(\mathbf{K}) &= \sum_{\mathbf{G}} e^{i\mathbf{G}\delta} H_{XX'}(\mathbf{K} + \mathbf{G}) \\
 &= \sum_{\mathbf{G}} \sum_{\Delta\delta} e^{i\mathbf{G}\delta} e^{-i(\mathbf{K}+\mathbf{G})(\Delta+\delta)} t_{XX'}(\Delta + \delta) \\
 &= \sum_{\Delta\delta} \delta_{\delta,\delta} e^{-i\mathbf{K}(\Delta+\delta)} t_{XX'}(\Delta + \delta) \\
 &= e^{-i\mathbf{K}\delta} \sum_{\Delta} e^{-i\mathbf{K}\Delta} t_{XX'}(\Delta + \delta).
 \end{aligned} \tag{3}$$

Here, reciprocal lattice vectors of the primitive cell/supercell are denoted by  $\mathbf{g} = b_1\mathbf{g}_1 + b_2\mathbf{g}_2$  and  $\mathbf{G} = \tilde{b}_1\mathbf{G}_1 + \tilde{b}_2\mathbf{G}_2$ , respectively. In practice, the supercell Hamiltonian can therefore be constructed by setting up the microscopic Hamiltonian  $H_{XX'}(\mathbf{k})$  on an equidistant mesh with  $n_s \times n_s$  momentum points that is shifted by the mini-BZ momentum  $\mathbf{K}$ . An inverse Fourier transform (in conjunction with a proper unraveling of the  $4n_s^2$  indices associated with the microscopic carbon  $p_z$ -orbitals that reside within the supercell) then yields the supercell Hamiltonian defined in Eq. (3). We note that the supercell Hamiltonian obtained by virtue of Fourier transformations differs in its gauge compared to the Wannier Hamiltonian defined in Eq. (2). This is because the Fourier transformation in Eq. (2) does not involve the (microscopic) positions of the carbon atoms within the primitive cell  $\mathbf{r}_X$  such that eigenstates of the Hamiltonian obey momentum space periodicity via  $\psi_{\mathbf{k}+\mathbf{g},b}(\mathbf{r}) = \psi_{\mathbf{k},b}(\mathbf{r})$ . The phase factor  $\exp(-i\mathbf{K}\delta)$  in the definition of the supercell Hamiltonian violates aforementioned momentum space periodicity, which however can be restored explicitly by a unitary gauge transformation.

The bandstructure for supercells with different choices of the scaling factor  $n_s$  is shown in Fig. 1 along the irreducible path of the concomitant mini-BZ. The red line indicates the position of the van-Hove singularity. The Wannierization scheme proposed in the main text remains valid as long as two single bands (one per valley) contribute to the Fermi surface, which marks a breakdown criterion at  $n_s \sim 60$ , i.e. where the supercell lattice constant  $L_s \sim 1/|\mathbf{q}_s|$  becomes comparable to the extend of the Fermi surface pockets at low electronic densities. For larger scaling factors additional bands appear in the vicinity of the Fermi energy requiring further supercell Wannier functions to capture their spectral weight.

## II. SUPERCELL WANNIERIZATION VIA SINGLE-SHOT PROJECTION

While implementations of the maximally localized Wannier function algorithm are readily available (e.g., Wannier90 [96]), creating symmetry adapted, maximally localized Wannier orbitals is in general more intriguing [92, 93]. We found that it is sufficient and more reliable<sup>1</sup> to construct Wannier functions manually by virtue of single-shot projections [68, 78, 94]. To this end, we consider a set of  $J_{\mathbf{k}}$  Bloch bands, which we would like to find a Wannier representation for. If all target bands are isolated,

<sup>1</sup> We apply the particular Wannierization procedure outlined in this section to models with large unit cells (supercells), i.e., thousands of orbitals in a tight-binding formalism. It therefore requires optimized code to tackle the computational demand.

exactly  $J_k = N_\alpha$  Wannier orbitals are required to represent all bands in the target band manifold. However, Wannier functions can also be sampled from a larger set of Bloch bands  $J_k > N_\alpha$  within a given energy window, c.f. Fig. 1 (c) of the main text. In this case, the number of target Bloch states may additionally vary for each crystal momentum  $\mathbf{k}$ . We then start from  $N_\alpha$  trial wavefunctions  $g_{k\alpha}(\mathbf{r})$ , which we project onto the target band manifold:

$$|\phi_{k\alpha}\rangle = \sum_{b \in J_k} w_{kb}^\alpha |\psi_{kb}\rangle \langle \psi_{kb} | g_{k\alpha} \rangle = \sum_{b \in J_k} A_{ab}(\mathbf{k}) |\psi_{kb}\rangle, \quad (4)$$

where  $w_{kb}^\alpha \in [0, 1]$  are optional weighting factors, which can be tuned to achieve optimal disentanglement of the bands. The matrix of inner products  $A_{ab}(\mathbf{k})$  is rectangular with dimension  $N_\alpha \times J_k$ . The projected wave functions  $|\phi_{k\alpha}\rangle$  are smooth in the momentum domain, but not orthonormal. Therefore, we next search for the best unitary approximation of  $A_{ab}(\mathbf{k})$  by performing an SVD  $\hat{A} = \hat{U} \hat{\Sigma} \hat{V}^\dagger$  of the overlap matrix and defining

$$\hat{B} = \hat{A} \left[ \hat{V} (\hat{\Sigma}^\dagger \hat{\Sigma})^{-1/2} \hat{V}^\dagger \right] = \hat{A} [\hat{A}^\dagger \hat{A}]^{-1/2}, \quad (5)$$

where all matrices above are evaluated at the same crystal momentum  $\mathbf{k}$ . By replacing  $A_{ab}(\mathbf{k})$  with its unitary approximation  $B_{ab}(\mathbf{k})$  in Eq. (4), we obtain Löwdin-orthonormalized states

$$|\chi_{k\alpha}\rangle = \sum_{\alpha=1}^{N_\alpha} B_{\alpha\beta}(\mathbf{k}) |\phi_{k\beta}\rangle, \quad (6)$$

which are related to the original Bloch states  $|\psi_{kb}\rangle$  by a unitary transformation. The orthonormalized states  $|\chi_{k\alpha}\rangle$  retain a smooth gauge in  $\mathbf{k}$  space and can therefore be cast to real-space Wannier functions by a (discrete) Fourier transformation.

For the graphitic models considered in the scope of this work, we find it convenient to do multiple iterations of the single-shot projection detailed above. Thereby we have the freedom of treating each *input* to an iteration as trial functions, allowing us to modify  $|\chi_{k\alpha}\rangle$  *before* the next iteration. We make use of this freedom by localizing the trial states with a Fermi cutoff, i.e.,

$$g(\mathbf{r}, \alpha) = f\left(\frac{|\mathbf{r}| - d}{\sigma}\right) \chi(\mathbf{r}, \alpha), \quad (7)$$

where  $d$  resembles the maximum spread of the new trial state,  $\sigma$  the decay width, and  $f(x) = (1 + e^x)^{-1}$  is the Fermi function. As weighting functions  $w_{kb}^\alpha$ , we choose asymmetric exponentials. The trial states corresponding to the conduction and valence bands, respectively, are weighted with

$$w_{kb}^\pm = \begin{cases} \exp\left(-\frac{|\epsilon_{kb} - E^\pm|}{\eta_{\text{intra}}}\right) & \text{iff } \epsilon_{kb} \in \epsilon^\pm, \\ \exp\left(-\frac{|\epsilon_{kb} - E^\mp|}{\eta_{\text{inter}}}\right) & \text{iff } \epsilon_{kb} \in \epsilon^\mp. \end{cases} \quad (8)$$

Here,  $\epsilon^\pm$  denotes the set of conduction (valence) bands, and  $E^\pm$  is the conduction (valence) band edge. The widths of the exponentials,  $\eta_{\text{intra}}$  and  $\eta_{\text{inter}}$ , determine whether the Haldane-like or a trivial Wannierization is found—we generally have to set  $\eta_{\text{inter}} > \eta_{\text{intra}}$  to achieve sufficient inter-orbital coupling, which is responsible for the topology.

### III. SUPERCELL WANNIER FUNCTIONS FOR BERNAL BILAYER GRAPHENE

In order to generate exponentially localized Wannier functions, we perform the modified single-shot projection technique detailed in Section II, with a Fermi function cutoff at scale  $d = 3L_s$  (with broadening  $\sigma = L_s/2$ ). The number of steps performed is four in total, with the first three steps including the Fermi smoothening, and the last step being a genuine projection of a trial function. We choose the symmetric (asymmetric) exponential energy cutoffs as  $\eta_{\text{intra}} = 0.1$  eV ( $\eta_{\text{inter}} = 0.18$  eV). Figure 2 (a) demonstrates that the resulting Wannier functions are exponentially localized. Most of the weight of the  $\zeta = +$  ( $\zeta = -$ ) Wannier orbital is concentrated on the non-dimer orbitals  $B_2$  ( $A_1$ ). In Fig. 2 (b), we further show the phase evolution of the supercell Wannier orbitals' envelope (i.e., canceling out the microscopic valley phase  $e^{i\mathbf{K}^\nu \cdot \mathbf{r}}$ ), where a phase winding of  $2\pi$  between the two sublattice components becomes apparent.



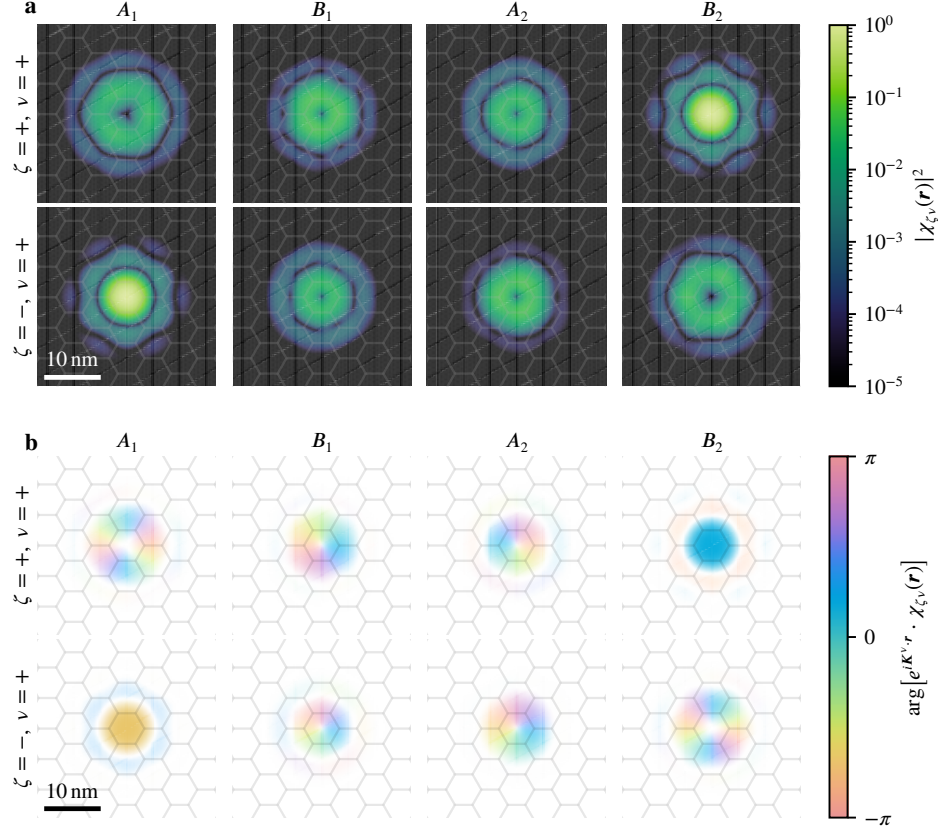


FIG. 2. Supercell Wannier functions of Bernal bilayer graphene under the influence of an electric displacement field  $\Delta = 60$  meV. (a): Absolute value of the two Wannier functions in real space for valley  $\nu = +$  on the four sublattices. (b) Complex phase evolution of the envelope function, i.e., without the microscopic phase stemming from the valley.

#### IV. SUPERCCELL WANNIER FUNCTIONS FOR MONOLAYER GRAPHENE

We model monolayer graphene with nearest- and next-nearest hopping parameters  $t = -2.7$  eV,  $t' = 0.1$  eV. We use a  $n_s \times n_s = 24 \times 24$  supercell, with a momentum resolution of  $N_k = 18^2$  points in the mini-BZ. The inversion symmetry breaking gap is added to the Hamiltonian as

$$H_\Delta = \Delta \sum_{\mathbf{r}} \left( c_{\mathbf{r},A_1}^\dagger c_{\mathbf{r},A_1} - c_{\mathbf{r},B_1}^\dagger c_{\mathbf{r},B_1} \right), \quad (9)$$

with  $\Delta = 50$  meV. In order to generate exponentially localized Wannier functions, we perform the modified single-shot projection technique detailed in Section II, with a Fermi function cutoff at scale  $d = 3L_s$  (with broadening  $\sigma = L_s/3$ ). The number of steps performed is four in total, with the first three steps including the Fermi smoothening, and the last step being a genuine projection of a trial function. The spread of the gaussian test function is set to  $0.3L_s$ , and the symmetric (asymmetric) exponential energy cutoff is  $\eta_{\text{intra}} = 0.05$  eV ( $\eta_{\text{inter}} = 0.15$  eV).

Figure 3 (a) demonstrates that the resulting Wannier functions are exponentially localized. Most of the weight of the  $\zeta = +$  ( $\zeta = -$ ) Wannier orbital is concentrated on the  $A_1$  ( $B_1$ ) sublattice. In Fig. 3 (b), we further show the phase evolution of the supercell Wannier orbitals' envelope (i.e., cancelling out the microscopic valley phase  $e^{i\mathbf{K}^\nu \cdot \mathbf{r}}$ ), where a phase winding of  $\pi$  between the two sublattice components becomes apparent. Panel (c) shows the resulting band structure of the projected model for valley  $\nu = +$  (orange) compared to the microscopic bandstructure in the supercell (i.e., *both* valleys; gray).

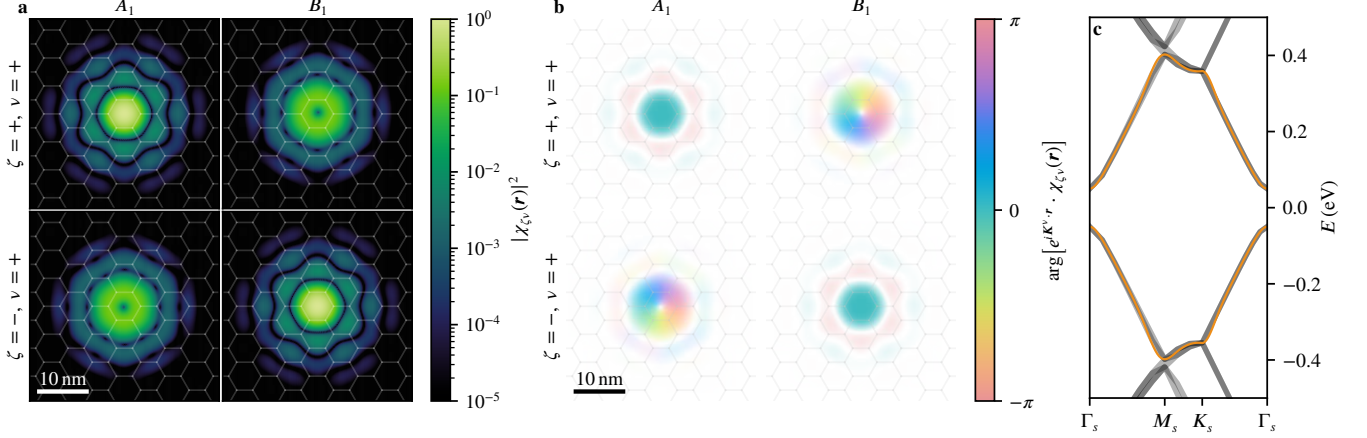


FIG. 3. Supercell Wannier functions of monolayer graphene under an inversion symmetry breaking field  $\Delta = 50$  meV. (a): Absolute value of the two Wannier functions in real space for valley  $\nu = +$ . (b): Complex phase evolution of the envelope function, i.e., without the microscopic phase stemming from the valley. (c): Band structure of the supercell model in *both* valleys (gray) and the wannierized model in valley  $\nu = +$  (orange).

## V. SUPERCELL WANNIER FUNCTIONS FOR RHOMBOHEDRAL (ABC) TRILAYER GRAPHENE

The microscopic Hamiltonian for rhombohedral (ABC) trilayer graphene is taken from Ref. [97]. We add inversion symmetry breaking  $\Delta$  via the following term in the Hamiltonian:

$$H_{\Delta} = \frac{3\Delta}{2} \sum_r \left( c_{r,A_1}^{\dagger} c_{r,A_1} + c_{r,B_1}^{\dagger} c_{r,B_1} - c_{r,A_3}^{\dagger} c_{r,A_3} - c_{r,B_3}^{\dagger} c_{r,B_3} \right), \quad (10)$$

with  $\Delta = 30$  meV. We choose  $n_s \times n_s = 18 \times 18$  as supercell size, with  $N_k = 24^2$  momentum points in the mini-BZ. The Fermi smoothening parameters are the same as in Section IV, as well as the energy/momentum space weighting parameters of the projected Wannier function guesses. Figure 4 (a) displays the absolute value of the two Wannier functions (for one valley  $\nu = +$ ) individually on each of the six sites in the microscopic unit cell. The evolution of the envelope phase is shown in Fig. 4 (b). Finally, Fig. 5 demonstrates that the Wannier functions accurately reproduce the dispersion of ABC trilayer graphene. We note that this plot shows *both* valleys of the microscopic model (gray), but only *one* valley of the Wannier model (orange).

## VI. DUAL-GATED OHNO-COULOMB INTERACTION

With Wannier functions defined on the microscopic  $p_z$  Wannier basis at hand, we may project the electronic Coulomb repulsion to the mesoscopic Wannier basis  $\chi_{\zeta,\nu}$ . First, we must define an appropriate interaction profile  $V(r)$  in real space. The long-range tail is screened exponentially in dual-gate setups of recent experimental device architectures [1, 6]:

$$V_{\text{long}}(r) = 4V_0 \sum_{k=0}^{\infty} K_0 \left[ (2k+1)\pi \frac{r}{\xi} \right], \quad (11)$$

where  $K_n(x)$  denotes a modified Bessel function of the second kind,  $V_0$  sets the overall interaction strength, and  $2\xi$  is the distance between the two gates [95]. The short-ranged part of the Coulomb interaction must also be screened when working with a lattice model. Thus we employ an Ohno potential [61]:

$$V_{\text{short}}(r) = \frac{U_0}{\sqrt{1 + r^2/a^2}}, \quad (12)$$

where we use  $U_0 = 8.3$  eV. Since the Ohno distance is on the order of  $a \sim 1$  Å, and gate distances are on the order of  $\xi \sim 10$  nm, we can safely assume to be in the limit where  $a/\xi \rightarrow 0$ .

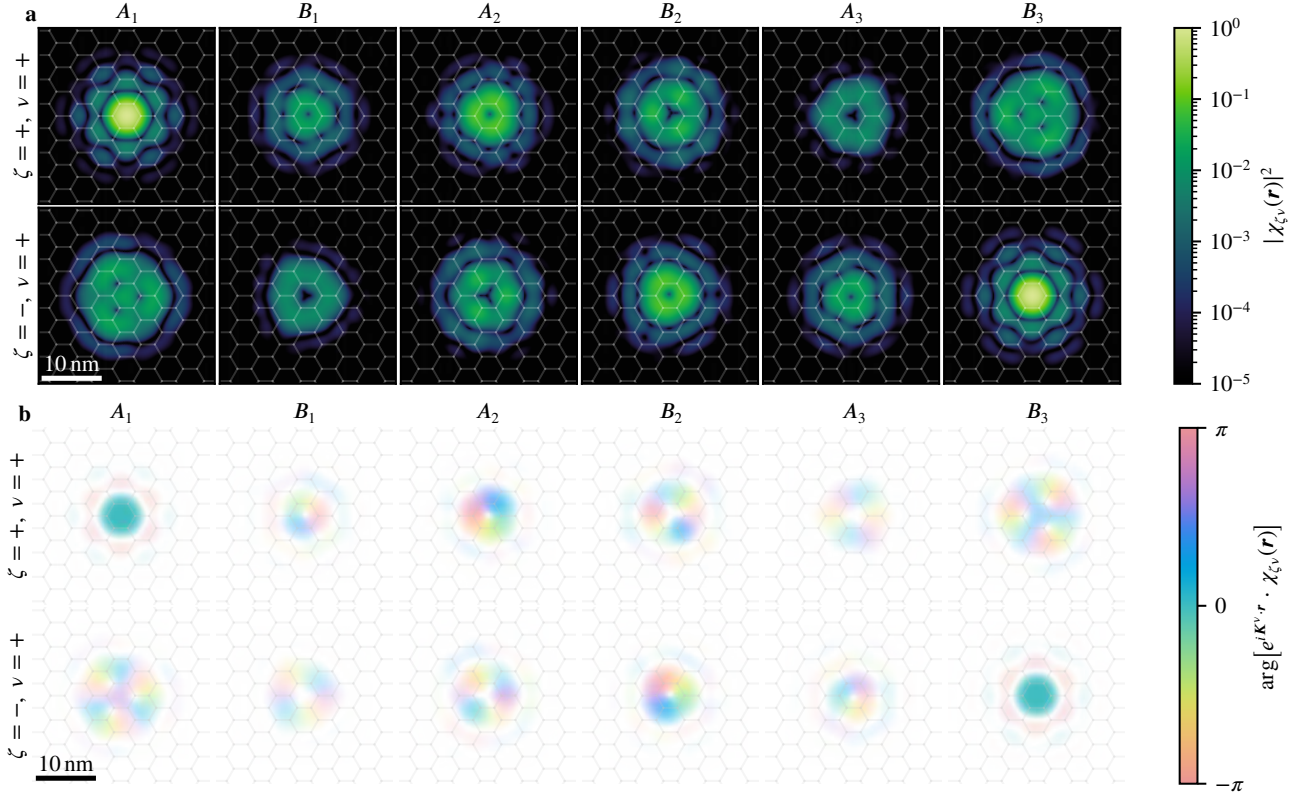


FIG. 4. Supercell Wannier functions of rhombohedral (ABC) trilayer graphene under the influence of an electric displacement field  $\Delta = 30$  meV. (a): Absolute value of the two Wannier functions in real space for valley  $v = +$  on the six sublattices. (b) Complex phase evolution of the envelope function, i.e., without the microscopic phase stemming from the valley.

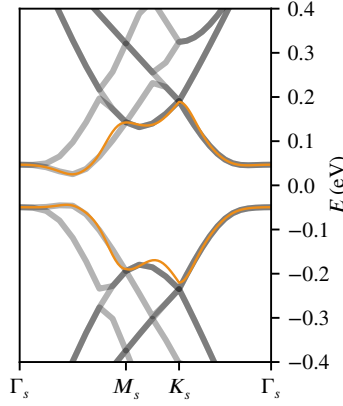


FIG. 5. Wannier interpolation (orange) of the supercell band structure (gray) of ABC trilayer graphene with  $\Delta = 30$  meV as perpendicular electric field.

Using the asymptotic properties of Eqs. (11) and (12),

$$V_{\text{long}}(r) \cdot \left( \frac{V_0 \xi}{r} \right)^{-1} = 1 + \mathcal{O} \left( \frac{r}{\xi} \right), \quad (13)$$

$$V_{\text{short}}(r) = \frac{U_0 a}{r} + \mathcal{O} \left( \frac{a^2}{r^2} \right), \quad (14)$$



we can replace  $r$  in Eq. (11) by its short-ranged screened expression motivated from Eq. (12), i.e.,

$$r_{\text{short}} = \sqrt{a^2 + r^2}. \quad (15)$$

Plugging this together, we have

$$V(r) = 4V_0 \sum_{k=0}^{\infty} K_0 \left[ (2k+1)\pi \frac{\sqrt{r^2 + a^2}}{\xi} \right], \quad (16)$$

which has the same long-range asymptotics as Eq. (11), and the same short-range behavior as Eq. (12), because the *long-range* behavior of Eq. (14) is just that of  $1/r$ , as well as the *short-range* behavior of Eq. (13).

In its final form, the Coulomb interaction Eq. (16) has no free parameters. The value of  $\xi$  is set by the (experimental) gate distance. Thereafter, we observe that the Hubbard- $U$  must be obtained at  $r = 0$ . Together with Eq. (13), this yields

$$U = V_0 \frac{\xi}{a}. \quad (17)$$

The energy scale of the long-range tail, however, is fixed by the dielectric constant  $\epsilon$ . Since  $\xi \gg a$ , there is a regime where  $\xi \gg r \gg a$ . In this regime, the interaction behaves in its regular Coulomb way. Thus, we can again use the asymptotic expansion Eq. (13) and compare it to the Coulomb interaction in a dielectric background (hBN,  $\epsilon \approx 4$ ):

$$V_0 \frac{\xi}{r} = \frac{\alpha}{\epsilon r}. \quad (18)$$

Equation (18) directly fixes  $V_0$ , and our sole choice to correctly reproduce the on-site Hubbard interaction  $U$  of graphitic systems is to modify the Ohno parameter  $a$  in a way that Eq. (17) is fulfilled. This yields

$$V_0 = \frac{\alpha}{\epsilon \xi}, \quad a = \frac{\alpha}{\epsilon U}. \quad (19)$$

Our approach of orbitally resolved supercell Wannier functions allows to capture more complicated interaction profiles, and there is no conceptual problem in using, e.g., a cRPA [88] (or cFRG [89]) interaction profile as an input for the downfolding procedure.

## VII. VALLEY AS QUANTUM NUMBER

In any microscopic (graphitic) lattice model, valley order must be encoded through an order parameter that lives on *bonds* rather than *sites*. This is due to the fact that the valley operator  $\mathcal{V}$  [77] intrinsically asks for hopping matrix elements rather than on-site components, i.e.,

$$\mathcal{V} = \frac{i}{3\sqrt{3}} \sum_{\langle\langle i,j \rangle\rangle} \eta_{ij} \sigma_z^{ij} c_i^\dagger c_j, \quad (20)$$

where  $\langle\langle i,j \rangle\rangle$  runs over all next-nearest (in-plane) neighbors,  $\eta_{ij}$  is  $\pm 1$  for (counter) clockwise direction, and  $\sigma_z$  acts in the space of sublattice (i.e.  $A, B$ ). In order to transform Eq. (20) to momentum space, we have to write it in terms of lattice vectors  $\mathbf{r}$ , sublattice indices  $i$ , and bonds  $\mathbf{b}_{r,i}^{r',j}$ . We show that the valley operator does *not* modulate the density, i.e., has no dependence on primary bilinear transfer momentum  $\mathbf{q}$ , but on the secondary momentum  $\mathbf{k}$ :

$$\mathcal{V} = \sum_{o \in \{A_1, \dots, B_N\}} \sigma_z^{oo} \frac{i}{3\sqrt{3}} \sum_{\mathbf{r}} \sum_{\mathbf{b}_{r,o}^{r',o}} \eta_b c_{r,o}^\dagger c_{\mathbf{r}+\mathbf{b},o} = \sum_{o \in \{A_1, \dots, B_N\}} \sigma_z^{oo} \frac{i}{3\sqrt{3}} \mathcal{V}_o \quad (21)$$

$$\begin{aligned} \mathcal{V}_o &= \sum_{\mathbf{r}, \mathbf{b}_{r,o}^{r',o}} \eta_b \sum_{\mathbf{k}} e^{-i\mathbf{k}\mathbf{r}} c_{\mathbf{k},o}^\dagger \sum_{\mathbf{k}'} e^{i\mathbf{k}'(\mathbf{r}+\mathbf{b}_{r,o}^{r',o})} c_{\mathbf{k}',o} = \sum_{\mathbf{k}, \mathbf{k}', \mathbf{r}, \mathbf{b}_{r,o}^{r',o}} e^{i\mathbf{k}'\mathbf{r}+i\mathbf{k}'\mathbf{b}_{r,o}^{r',o}-i\mathbf{k}\mathbf{r}} \eta_b c_{\mathbf{k},o}^\dagger c_{\mathbf{k}',o} \\ &= \sum_{\mathbf{k}, \mathbf{k}', \mathbf{r}, \mathbf{b}_o} e^{i\mathbf{k}'\mathbf{r}+i\mathbf{k}'\mathbf{b}_o-i\mathbf{k}\mathbf{r}} \eta_b c_{\mathbf{k},o}^\dagger c_{\mathbf{k}',o} = \sum_{\mathbf{k}, \mathbf{b}_o} e^{i\mathbf{k}\mathbf{b}} \eta_b c_{\mathbf{k},o}^\dagger c_{\mathbf{k},o} = \sum_{\mathbf{k}} \left( \sum_{\mathbf{b}_o} e^{i\mathbf{k}\mathbf{b}} \eta_b \right) c_{\mathbf{k},o}^\dagger c_{\mathbf{k},o} = \sum_{\mathbf{k}} \eta_{k,o} c_{\mathbf{k},o}^\dagger c_{\mathbf{k},o}, \end{aligned} \quad (22)$$

where we used the fact that the bonds  $\mathbf{b}_{r,i}^{r',j}$  only depend on the sublattice index  $o$ . Equation (22) suggestively expresses the valley operator in the language of a nematic bilinear (also known in the context of a Pomeranchuk instability), making it clear that it,

in terms of a general Fermion bilinear  $\langle c_{q+k}^\dagger c_k \rangle$ , represents a term that resides at  $q \equiv 0$ . It can thus *never* be formulated through an on-site bilinear, no matter what basis transformation is chosen.

However, we can approximate the valley operator with  $\mathcal{V}^Q$ :

$$\mathcal{V}^Q = \sum_{o \in \{A_1, \dots, B_N\}} \sigma_z^{oo} \frac{i}{3\sqrt{3}} \mathcal{V}_o^Q, \quad \mathcal{V}_o^Q = \sum_k \eta_{k,o} c_{k+Q,o}^\dagger c_{k,o}, \quad (23)$$

where  $|Q| \ll |g_i|$ , with  $g_i$  the reciprocal lattice vectors. Equation (23) now corresponds to a Fermion bilinear that, besides its bond content  $\eta_{k,o}$ , has a modulated “density” component at momentum scale  $Q$ . In the SWF language, we choose  $Q \in \{G_1, G_2, G_3\}$  as the mesoscopic reciprocal lattice vectors that satisfy  $|G_i| \ll |g_i|$ , since the extent of the supercell is  $n_s \gg 1$ . Because the *approximate* valley operator  $\mathcal{V}^Q$  drops to zero at the Brillouin zone edges, one can choose a basis *within one supercell* where it is diagonal. This is automatically encoded in our Wannier trial states, because we take Bloch states from the original  $K^\nu$  points. Truncating the Wannier basis after a fixed number of trial states renders valley a quantum number in the Wannier basis.  $U(1)$  valley symmetry of the projected model can therefore be understood to be *approximate* in the following sense: The valley operator is shifted from zero transfer momentum to  $0 < |Q| \ll |g_i|$ . Hence  $U(1)$  becomes exact only in the infinite supercell limit (the continuum limit).

- 
- [44] J. Jung and A. H. MacDonald, Accurate tight-binding models for the  $\pi$  bands of bilayer graphene, *Physical Review B* **89**, 035405 (2014).
  - [96] A. A. Mostofi, J. R. Yates, Y.-S. Lee, I. Souza, D. Vanderbilt, and N. Marzari, wannier90: A tool for obtaining maximally-localised wannier functions, *Computer physics communications* **178**, 685 (2008).
  - [93] K. Koepnick, O. Janson, Y. Sun, and J. Van Den Brink, Symmetry-conserving maximally projected wannier functions, *Physical Review B* **107**, 235135 (2023).
  - [92] M. Kang, S. Fang, L. Ye, H. C. Po, J. Denlinger, C. Jozwiak, A. Bostwick, E. Rotenberg, E. Kaxiras, J. G. Checkelsky, and R. Comin, Topological flat bands in frustrated kagome lattice CoSn, *Nature Communications* **11**, 4004 (2020).
  - [78] N. Marzari and D. Vanderbilt, Maximally localized generalized wannier functions for composite energy bands, *Physical review B* **56**, 12847 (1997).
  - [94] I. Souza, N. Marzari, and D. Vanderbilt, Maximally localized wannier functions for entangled energy bands, *Phys. Rev. B* **65**, 035109 (2001).
  - [68] S. Carr, S. Fang, H. C. Po, A. Vishwanath, and E. Kaxiras, Derivation of wannier orbitals and minimal-basis tight-binding hamiltonians for twisted bilayer graphene: First-principles approach, *Phys. Rev. Res.* **1**, 033072 (2019).
  - [97] F. Zhang, B. Sahu, H. Min, and A. H. MacDonald, Band structure of *abc*-stacked graphene trilayers, *Phys. Rev. B* **82**, 035409 (2010).
  - [6] A. M. Seiler, M. Statz, I. Weimer, N. Jacobsen, K. Watanabe, T. Taniguchi, Z. Dong, L. S. Levitov, and R. T. Weitz, Interaction-driven (quasi-) insulating ground states of gapped electron-doped bilayer graphene (2023), [arXiv:2308.00827 \[cond-mat.str-el\]](https://arxiv.org/abs/2308.00827).
  - [1] A. M. Seiler, F. R. Geisenhof, F. Winterer, K. Watanabe, T. Taniguchi, T. Xu, F. Zhang, and R. T. Weitz, Quantum cascade of correlated phases in trigonally warped bilayer graphene, *Nature* **608**, 298 (2022).
  - [95] R. E. Throckmorton and O. Vafek, Fermions on bilayer graphene: Symmetry breaking for  $b=0$  and  $v=0$ , *Physical Review B* **86**, 115447 (2012).
  - [61] T. O. Wehling, E. Şaşıoğlu, C. Friedrich, A. I. Lichtenstein, M. I. Katsnelson, and S. Blügel, Strength of effective coulomb interactions in graphene and graphite, *Phys. Rev. Lett.* **106**, 236805 (2011).
  - [88] F. Aryasetiawan, M. Imada, A. Georges, G. Kotliar, S. Biermann, and A. Lichtenstein, Frequency-dependent local interactions and low-energy effective models from electronic structure calculations, *Physical Review B* **70**, 195104 (2004).
  - [89] M. Kinza and C. Honerkamp, Low-energy effective interactions beyond the constrained random-phase approximation by the functional renormalization group, *Phys. Rev. B* **92**, 045113 (2015).
  - [77] A. Ramires and J. L. Lado, Electrically tunable gauge fields in tiny-angle twisted bilayer graphene, *Physical review letters* **121**, 146801 (2018).